

MIT Open Access Articles

Modeling Lithium Plating Onset on Porous Graphite Electrodes Under Fast Charging with Hierarchical Multiphase Porous Electrode Theory

The MIT Faculty has made this article openly available. **Please share** how this access benefits you. Your story matters.

Citation: Huada Lian and Martin Z. Bazant 2024 J. Electrochem. Soc. 171 010526

As Published: 10.1149/1945-7111/ad1e3d

Publisher: The Electrochemical Society

Persistent URL: <https://hdl.handle.net/1721.1/157423>

Version: Final published version: final published article, as it appeared in a journal, conference proceedings, or other formally published context

Terms of use: Creative Commons Attribution





Modeling Lithium Plating Onset on Porous Graphite Electrodes Under Fast Charging with Hierarchical Multiphase Porous Electrode Theory

Huada Lian¹ and Martin Z. Bazant^{1,2,z}

¹Department of Chemical Engineering, Massachusetts Institute of Technology, Cambridge, Massachusetts 02139-4307, United States of America

²Department of Mathematics, Massachusetts Institute of Technology, Cambridge, Massachusetts 02139-4307, United States of America

Lithium plating during fast charging of porous graphite electrodes in lithium-ion batteries accelerates degradation and raises safety concerns. Predicting lithium plating is challenging due to the close redox potentials of lithium reduction and intercalation, obscured by the nonlinear dynamics of electrochemically driven phase separation in hierarchical pore structures. To resolve dynamical resistance of realistic porous graphite electrodes, we introduce a model of porous secondary graphite particles to the multiphase porous electrode theory (MPET), based on electrochemical nonequilibrium thermodynamics and volume averaging. The resulting computational framework of “hierarchical MPET” is validated and tested against experimental data over a wide range of fast charging conditions and capacities. With all parameters estimated from independent sources, the model is able to quantitatively predict the measured cell voltages, and, more importantly, the experimentally determined capacity for lithium plating onset at fast 2C to 6C rates. Spatial and temporal heterogeneities in the lithiation of porous graphite electrodes are revealed and explained theoretically, including key features, such as idle graphite particles and non-uniform plating, which have been observed experimentally.

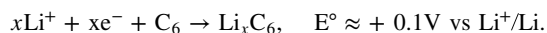
© 2024 The Author(s). Published on behalf of The Electrochemical Society by IOP Publishing Limited. This is an open access article distributed under the terms of the Creative Commons Attribution 4.0 License (CC BY, <http://creativecommons.org/licenses/by/4.0/>), which permits unrestricted reuse of the work in any medium, provided the original work is properly cited. [DOI: 10.1149/1945-7111/ad1e3d]



Manuscript submitted September 22, 2023; revised manuscript received November 27, 2023. Published January 24, 2024.

Supplementary material for this article is available [online](#)

Fast charging of conventional lithium-ion batteries (LIB) is desirable but practically constrained by degradation and safety concerns related to electrochemical deposition of lithium metals on graphite anodes, i.e. lithium plating.¹ The intrinsic challenge of fast charging while avoiding lithium plating stems from the small difference of redox potentials between the reduction of lithium ions and insertion of lithium ions into graphite,



Lithium plating on graphite becomes thermodynamically allowed in the region where electrode voltage with respect to lithium metal drops below 0 V. Given the practical difficulty of measuring voltage locally inside a porous electrode of typical thickness about 50 μm , experimental efforts have primarily focused on promptly detecting lithium plating by measuring its side effects, such as changes of resistance/impedance,^{2–5} differential voltage,^{6,7} coulombic efficiency,^{8,9} and pressure/volume.^{10,11} Therefore, it is of interest to approach this problem from a computational perspective to determine onset of lithium plating.

Precise tracking of the local potential is pre-requisite for determining the onset of lithium plating, along with a realistic model for the reaction kinetics. This is computationally challenging in porous graphite electrodes because it requires the resolution of both transport resistance and faradaic resistance simultaneously and accurately in a porous media. Previous simulations based on porous electrode theory (PET) have focused on resolving transport resistance in electrode scale and treated lithium-graphite compounds as solid solutions, offering qualitative insights into the trend of onset of lithium plating as a function of electrolyte transport property,¹² electrode tortuosity,¹³ and electrode capacity.^{14–17} However, Li_xC_6 exhibits at least two phase-separation regimes,¹⁸ within each of which reaction resistance and solid diffusion resistance change substantially.^{19,20} As Li inserts into graphite, phase-separation arises from the multiple free energy minima resulting in stage shapes in

open-circuit voltage within the window of phase-separation.²⁰ Lithium ions preferentially localize in layers between graphene planes, leading to the naming convention of stages based on the number of graphene layers between each Li-rich domain. For example, Stage I corresponds to the fully lithiated LiC_6 , characterized by Li-graphene-Li alternating layer structure, and Stage II corresponds to LiC_{12} featuring two graphene planes separating adjacent lithium layers.²¹ Recently, nontrivial lithiation dynamics of porous graphite electrodes, such as idle graphite particles under intermediate current and three phases coexisting in high rates, has been identified by in-operando optical experiments²² and XRD.²³ As a result, the faradaic resistance of graphite particles is inherently dynamical and heterogeneous due to driven phase separation.

Multiphase porous electrode theory (MPET)²⁴ based on porous electrode theory²⁵ applies nonequilibrium thermodynamics with material-specific free energy functionals to capture the impact of phase separation in batteries. The underlying phase-field models have been shown to replicate the phase boundary propagation in single particle of Li_xFePO_4 and Li_xC_6 ,^{19,26–28} as well as the propagation of stages of Li_xC_6 across the porous electrode, as observed in experiments.^{28,29} While several successful simulations using phase-field models similar to MPET have been reported recently,^{29–31} these are limited to relatively low currents, in which transport limitations have not played a significant role.

Furthermore, past simulations have lacked the precision required to clearly delineate the dynamic contributions arising from the particle size distribution and hierarchical pore structures, which are often characteristics of porous graphite electrodes. Graphite particles typically consist of submicron-size graphitic domains aggregated or compressed into micron-sized particles, known as secondary particles. Despite their low particle porosity, graphite secondary particles from various sources typically possess a specific surface area about $1 - 2 \text{ m}^2 \text{ g}^{-1}$,^{32–34} which is several times that of a solid graphite sphere with a typical diameter $10 \mu\text{m}$ ($\sim 0.2 \text{ m}^2 \text{ g}^{-1}$). Therefore, substantial amount of reactions can take place within the porous particle. Similar secondary structure exists for other electrode materials, leading to the development of a hierarchical porous electrode theory with two level of pores.^{35,36} A unified model

^zE-mail: bazant@mit.edu

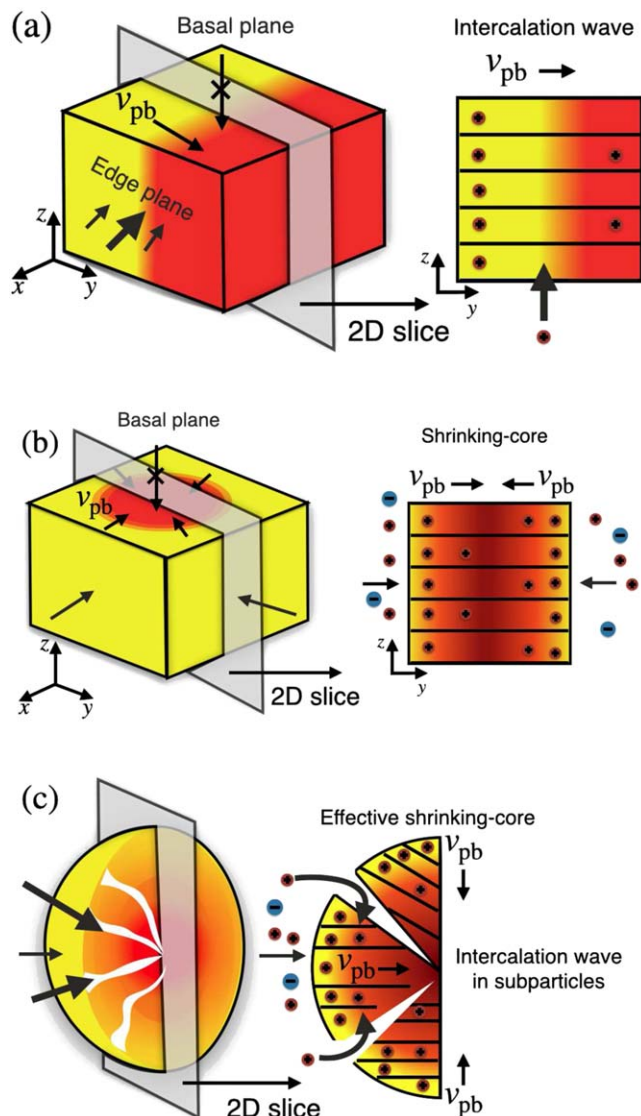


Figure 1. Ion intercalation and phase morphology of single crystal graphite and secondary graphite particle. v_{pb} denotes the direction of phase boundary movement. Edge planes of graphite on the sides of single crystals (a), (b) are accessible to ion intercalations, while basal planes on top and bottom surfaces of graphite crystals (a), (b) are not. (a) Intercalation wave in single crystal under low current. (b) Shrinking-core pattern in single crystal under high current. (c) Porous graphite particle permits only intercalation wave in each subparticle due to depletion of electrolytes inside porous particle resulting in the effective shrinking-core pattern. Ion concentration of the example graphite particles are within the regime of Stage II(red)-I(yellow) coexistence.

resolving both multiphase and multiscale dynamics simultaneously remains lacking.

In this work, we introduce “hierarchical multiphase porous electrode theory” and apply it to the fundamental problem of lithium plating onset in fast charging of porous graphite anodes in Li-ion batteries. We focus on capturing the effects of phase-separation, multiscale porosity, and secondary particle size distribution on the lithiation dynamics and plating onset of realistic graphite anodes. The general framework of Hierarchical MPET and various algorithms for its efficient implementation in the MPET open-source software package³⁷ will be described in a companion paper.

The next two sections present the details of the simulation model and validate the model against experiments of Li/graphite half cells under various fast charging conditions.⁸ The spatial and temporal

dynamics of lithiation of porous graphite electrode are drawn from simulations, followed by a brief summary of our findings.

Simulation Model

The model for porous graphite electrodes considered here is based on an extension to porous electrode theory,^{24,25} featuring a coarse-grained model that captures the multiscale transport and the multiphase feature of a porous graphite particle. In a porous secondary graphite particle, two ion insertion pathways exist as illustrated in Fig. 1c: one involving the solid pathway where Li^+ is intercalated on outermost surfaces, and the other involving a liquid pathway where Li^+ moves into micropores within particles before being intercalated through inner surfaces.

We begin by introducing the phase-field approach for a single crystal graphite and then extend it to a porous secondary graphite particle.²⁵ Then, we revisit volume averaging in porous electrode theory²⁵ to explicitly incorporate the particle size distribution of secondary particles. Lastly, we introduce the reaction kinetic models used in the following simulations for intercalation and lithium plating/stripping. Our model is implemented as an extension of our previously developed Multiphase Porous Electrode Theory (MPET) package.²⁴

Model of single crystal graphite particle.—We start with introducing the phase-field approach for the phase-separable single crystal graphite. Phase separation emerges from minimizing free energy in the presence of a multi-well free energy landscape, leading to nonuniform distribution on the surface of equilibrium phase and phase boundary regions. The generalized Cahn-Hilliard reaction model derived from nonequilibrium thermodynamics (Eq. 56 in Ref. 38) describes the phase separation process by a mass balance equation at any point \mathbf{r} as a result of mass flux driven by the gradient of chemical potential μ and reactions $R(c)$ as following

$$\frac{\partial c(\mathbf{r})}{\partial t} = \nabla \cdot (D_i(c) \nabla \tilde{\mu}(\mathbf{r})) + R(c), \quad [1]$$

where c and D_i are the concentration and tracer diffusivity of the concerned species, respectively. $\tilde{\mu} \equiv \mu/(k_B T)$ is chemical potential nondimensionalized by the thermal energy $k_B T$.

For a single crystal of layered materials like graphite and Li_xCoO_2 depicted in Fig. 1a, ions diffuse preferentially along the 2D basal planes (e.g. planes parallel to graphene sheets) and insert into the solid only through the edge planes exposed to electrolytes (e.g. planes perpendicular to graphene sheets). Equation 1 can be reduced to a 2D model by averaging solid concentrations in the multilayer structure to one averaged concentration.^{20,26,29} It describes the phase morphology under nonequilibrium conditions as following

$$\frac{\partial c(x, y)}{\partial t} = \nabla \cdot (D_i c(x, y) \nabla \tilde{\mu}(x, y)), \quad j = -D_i c \nabla \tilde{\mu} \cdot \hat{n}, \quad [2]$$

where j is the faradaic reaction rate on the surface and \hat{n} is the normal unit vector of the surface. A finer model considering multiple layers is possible by coupling Eq. 2 for each layer with appropriate free energy functional but computationally prohibitive in simulations of porous electrodes.^{20,39}

When all surfaces of the crystal have equal accessibility to the electrolytes, the phase morphology of graphite and Li_xCoO_2 using Eq. 2 has been found to be current dependent.^{40,41} Intercalation wave patterns as shown in Fig. 1a are observed under low current, in which ion insertion takes place preferentially on the phase boundary due to the higher exchange current density and free energy density at phase boundaries.^{40,42} While under high current conditions, shrinking-core patterns with the slow diffusion phase filling the outer surfaces of the compact particle as depicted in Fig. 1b have been observed, leaving phase boundaries inaccessible to the

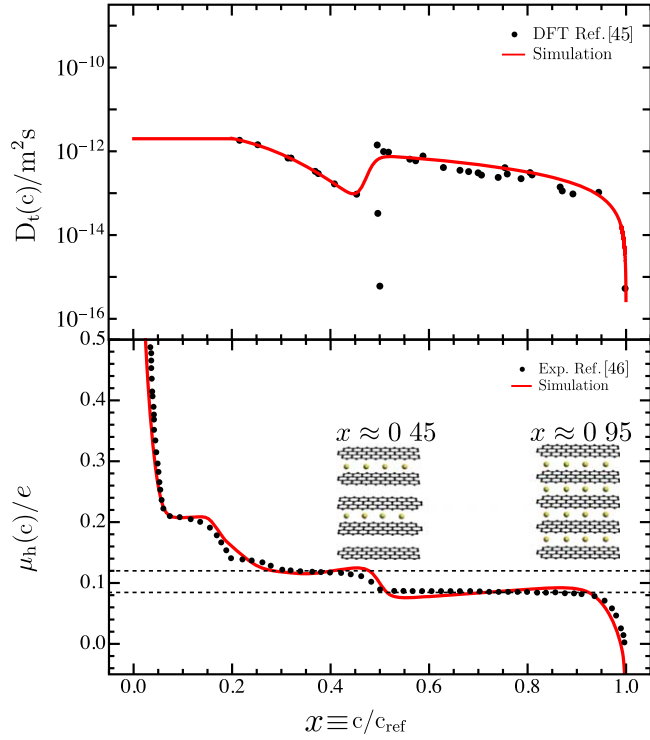


Figure 2. (Top) The concentration dependent tracer diffusivity $D_t(c)$ of Li^+ in graphite adapted from density functional theory calculations.⁴⁵ (Bot) The homogeneous part of chemical potential $\mu_h(c)$ for Li-graphite system displays multiple stages. The functional form is adapted from the open-circuit voltage of Li_xC_6 , defined as $eV_{\text{Li}_x\text{C}_6}^{\text{OCV}} = \mu_{\text{Li}_x\text{C}_6} - \mu_{\text{Li}}^0$ with respect to Li metal reference electrode.⁴⁶

electrolytes.^{19,26,40,43} These different phase morphologies are the emerging results of competing time scales of reactions prescribed by the applied current and diffusion of the slowest phase determined by the materials property. The phase morphology of a particle together with the particle porosity determines the distribution of reactions in a porous graphite particle.

Model of single secondary graphite particle.—Secondary particles possess particle porosity, enabling electrolyte access to inner pores, as depicted in Fig. 1c. Phase boundaries within the secondary particle thus permit ion intercalations, even under high current conditions. In contrast to the shrinking-core pattern of a compact particle solely driven by solid diffusion as shown in Fig. 1b, secondary particles are expected to exhibit an effective shrinking-core pattern because the phase boundaries are driven by both solid diffusion and ion intercalations on phase boundaries through reactions in pores within secondary particles. Depending on the orientation of crystalline domains, the secondary particle can be modeled as either a sphere or a cylinder to best match the electrode morphology.^{43,44} If the outer surface is primarily composed of edge planes, a sphere is more appropriate. Conversely, if basal planes contribute significantly to the outer surfaces, a cylinder is better. We choose the spherical model below only to be comparable with experiments.

The effective shrinking-core pattern thereby allows us to approximate phase boundary movement in the solid phase of a secondary particle using a 1D radial reaction-diffusion model adapted from Eq. 1 by volume averaging of Eq. 1 over a spherical shell at radius r .

$$(1 - \epsilon^p) \frac{\partial \langle c \rangle(r)}{\partial t} = \nabla \cdot [D_t \langle c \rangle \nabla \tilde{\mu}(\langle c \rangle)] + \langle R(c) \rangle, \quad j = -D_t \langle c \rangle \nabla \tilde{\mu}(\langle c \rangle) \cdot \hat{n}. \quad [3]$$

Here, $\langle c \rangle(r)$ defines a volume averaged solid concentration over a spherical shell at radius r . ϵ^p denotes the particle porosity and $1 - \epsilon^p$ appears on the left because volume averaging is only taken over the solid part of secondary particle. The argument of $\langle c \rangle$ on the right are implicit only for the purpose of clarity. Although mathematically similar to Eq. 1, their physical meaning are different. The first term on the right is the mass flux along radial direction averaged across multiple crystals, driven by the averaged concentration $\langle c \rangle$ and corresponding chemical potential gradient. The second reaction term $\langle R(c) \rangle$ is physically distinct from the bulk reaction in Eq. 1 in the sense that it represents all surface reactions on exposed edge planes in the volume of the shell located at r due to particle porosity. Here, $D_t(\langle c \rangle)$ and $\mu(\langle c \rangle)$ are concentration dependent and remain their respective functional forms as they are depicted in Fig. 2 for single crystals considering the high graphitic degree in typical graphite materials.

The chemical potential $\mu(c)$ is generally expressed as $\mu(c) = \mu_h(c) - \kappa \nabla^2 c$, where μ_h is the homogeneous part of chemical potential and κ quantifies the free energy penalty of phase-boundaries. The homogeneous chemical potential $\mu_h(c)$ for graphite is adapted from the open-circuit voltage as shown in Fig. 2. Physically, it represents the lithium-carbon and lithium-lithium interactions, resulting in a multi-well free energy landscape that drives phase separation.²⁰ $x \equiv c/c_{\text{ref}} \in [0, 1]$ is the lithiation extent in Li_xC_6 where c_{ref} is the theoretical capacity of graphite. Phase separation occurs in our model at concentration between $x \approx 0.33$ (stage III) and $x \approx 0.45$ (stage II) corresponding to the Stage III-II coexistence, and between $x \approx 0.5$ (stage II) and $x \approx 0.95$ (stage I) for the Stage II-I coexistence. The region with lower concentration is treated as a solid solution, ignoring all low stoichiometry phases below $x < 0.33$. The DFT calculated tracer diffusivity is adapted and used in our model. A constant diffusivity assumption for the missing concentration when $x < 0.2$ is made. We further replace the DFT calculated extremely low diffusivity at $x = 0.5$ with a continuous jump around $x \approx 0.5$ to match the phase transition to Stage I, considering that lithium ions are allowed to move in the newly opened empty layer through multiple kinds of defects during the transition from stage II to stage I.²¹ Notably, the tracer diffusivity from DFT displays $(0.5 - x)$ dependence when $0.2 < x < 0.5$ and $(1 - x)$ dependence when $0.5 < x < 1.0$, similar to a lattice site exclusion argument near stage II and stage I.⁴⁷ Expressions for the DFT fitted diffusivity and chemical potential in Fig. 2 can be found in SI.

To demonstrate the coupling of ion concentrations in the solid phase and the liquid phase, Eq. 3 is reproduced in the form of general continuity equation using Eq. 4a together with the continuity equation governing the ion concentration in the liquid phase using Eq. 4b. The effective ionic transport of lithium ions in the electrolyte inside pores of secondary particles is treated in the same manner as that in the electrode scale.⁴⁸ This involves utilizing Stefan-Maxwell concentrated electrolyte theory and the effective medium theory for effective transport in porous media(SI).²⁴ The averaged quantities, such as ion concentration $\langle c_+ \rangle^p$ and ion flux in liquid $\langle F_+ \rangle^p$, are defined at the particle scale with superscript “p” to be distinguished from those averaged quantities defined at the electrode scale. In the shell located at radius r , averaged concentration of ions in liquids $\langle c_+ \rangle^p$ and the averaged concentration of ions in solids $\langle c \rangle$ are governed by following continuity equations using the finite volume method

$$\epsilon^p V_s(r) \frac{\partial \langle c_+ \rangle^p(r)}{\partial t} = -\nabla \cdot (\langle F_+ \rangle^p A_s(r)) + i a V_s(r), \quad [4a]$$

$$(1 - \epsilon^p) V_s(r) \frac{\partial \langle c \rangle(r)}{\partial t} = -\nabla \cdot (\langle F \rangle^p A_s(r)) - i a V_s(r). \quad [4b]$$

Here, $\langle F_+ \rangle^p$ and $\langle F \rangle^p = -D_t \langle c \rangle \nabla \tilde{\mu}(\langle c \rangle)$ are the average flux of lithium ions in micropores and in the solid, respectively. The average

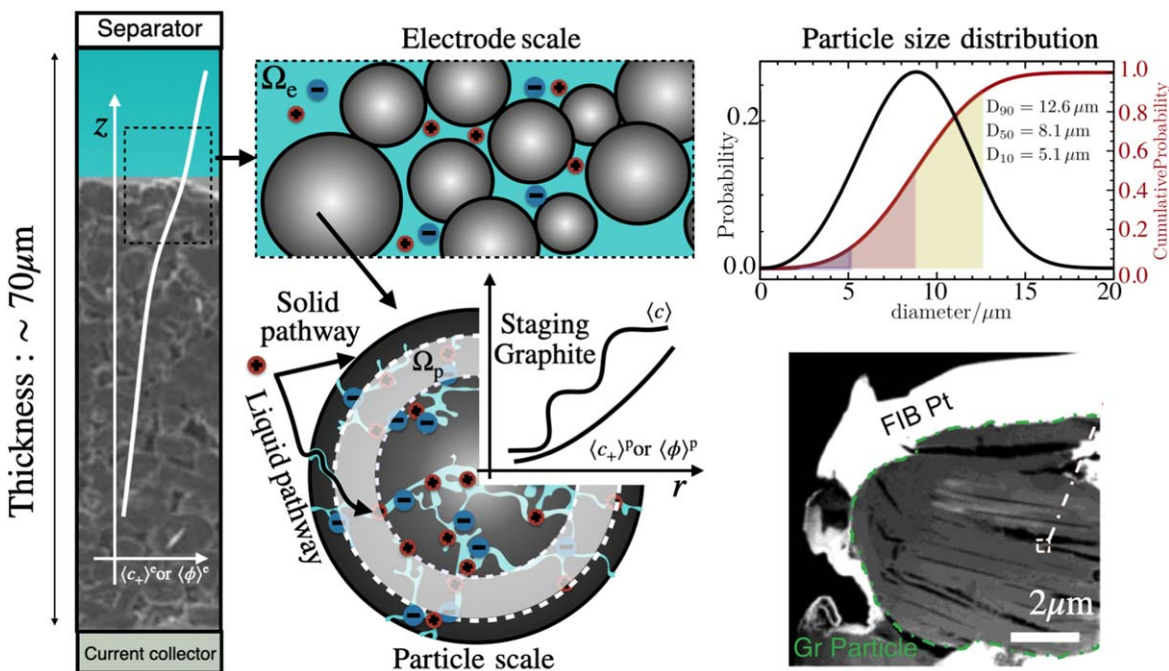


Figure 3. Schematics of the hierarchical multiphase porous electrode theory and morphology of porous electrode and porous particle. Particle size distribution is accounted for in the electrode scale averaging. Interplay of solid pathway and liquid pathway is accounted for in the particle scale averaging. Images of the cross section of porous electrode and a secondary porous graphite particle are adapted from J. Elec. Soc.⁴⁴ with permission.

flux of cations $\langle F_+ \rangle^p$ in pores within particles can be evaluated using Eq. S1 for electrode scale transport by substituting the porosity ϵ^e and tortuosity τ^e of the electrode with those of particles, i.e. ϵ^p and τ^p . V_s and A_s are the volume and cross-sectional surface areas of the shell. Given the diameter of pores in particle varying from tens nanometers to hundreds nanometers, the effective transport properties of electrolytes in nanoscale pores is likely to be impacted by the presence of solid electrolyte interphase (SEI), whose thickness is of order of ~ 50 nm. Therefore, the porosity and tortuosity for determining the effective diffusivity and conductivity within micropores are material-specific fitted parameters in practice.

In a secondary particle, the transport of ions in both the liquid and solid is coupled through the reaction terms on the right of Eq. 4. The areal faradaic current density i (mA cm^{-2}) denotes the faradaic reactions on the inner surfaces of micropores depending on cation concentration $\langle c_+ \rangle^p$ and electrochemical potential of Li^+ locally at radius r . The kinetic model governing faradaic reactions inside particle is identical to those for the outer surface, which is described in subsection Kinetic model of electrochemical reactions above. a is the volumetric reactive surface area from pores within secondary particles determined from the BET specific surface area. (See SI) We do not further distinguish areas of the basal planes and edge plans in a . Thus, $aV_s(r)$ amounts to the reactive surface in the shell located at r .

The boundary conditions that couple the electrolyte transport inside porous particles and that in the electrode are two continuity conditions of cation concentrations $\langle c_+ \rangle$ and electrochemical potential of Li^+ on the surface of particle. We refer details of the finite volume method to previous works.^{24,49} While the phase-field model for simulating graphite^{24,47} and porous particle model^{36,50,51} have been previously developed, this work stands out as the first to unify them. As a result, the model is capable of describe the dynamic resistance arising from the interplay of phase-separation and particle porosity, making it suitable for all layered multiphase materials having a secondary structure.

Modeling particle size distribution in a porous electrode.—In this section, the secondary graphite model introduced previously is

combined with the porous electrode theory considering a particle size distribution explicitly. Figure 3 illustrates the two levels of volume averaging in this hierarchical multiphase porous electrode theory. Our model at the electrode scale differs from previous ones by directly incorporating the particle size distribution in the porous electrode scale. Previous works using PET and MPET are typically limited to simulate single or few particle sizes in each electrode volume.^{24,28,52,53}

We consider N spherical particles in a chosen volume element Ω^e in the electrode.

Defining for any quantity its volume average $\langle x \rangle^e \equiv V(\Omega^e)^{-1} \int_{\Omega^e} x \, dV$ within Ω^e . The superscript “e” implies averaging at the electrode scale. Considering the large area of the electrode sheet, the volume averaged concentration of cations $\langle c_+ \rangle^e$ along the thickness direction of a porous electrode is governed by the following mass balance equation⁴⁸

$$\epsilon^e \frac{\partial \langle c_+ \rangle^e}{\partial t} = \nabla \cdot \langle F_+ \rangle^e + V^{-1} \sum_i^N \int_{A_i} j_i \, dA, \quad [5]$$

where subscript “ i ” denotes the i th particle. Porosity ϵ^e appears as $c_+(r)$ is nonzero only in the pore region. $\langle F_+ \rangle^e$ denotes the average flux of the cation over a cross section through the porous electrode. Fundamental transport processes in porous media and concentrated electrolytes for evaluating $\langle F_+ \rangle^e$ are provided in the SI and previous works.^{24,48}

The second term on the right side of Eq. 5 represents the sum of the areal ionic current density j_i on all particle surfaces including the contribution from both the liquid pathway and the solid pathway as shown in Fig. 3. In this work, j_i is uniformly distributed across the surface of each particle due to the following two approximations: (1) Via volume averaging in electrode, particles in Ω^e are in contact with electrolytes with a uniform cation concentration $\langle c_+ \rangle$ as previous porous electrode theory works,^{24,25} and (2) Our utilization of the spherical particle model. We can rewrite the sum over N particles as a weighted-sum based on a particle size distribution $n(R)$

$$e^e \frac{\partial \langle c_+ \rangle^e}{\partial t} = \nabla \cdot \langle F_+ \rangle^e + V^{-1} \sum_i^{N_R} n(R_i) 4\pi R_i^2 j_i. \quad [6]$$

Here, we discretize the continuous distribution $n(R)$ into N_R intervals, where R_i and $n(R_i)$ represent the radius and number density of the i th interval, respectively. In SI, we employ the notation of spatial decomposition⁵⁴ to analyze the error associated with the reactive term in Eq. 2, which remains small when concentration gradient of ions in electrolytes is small.

Kinetic model of electrochemical reactions.—For the faradaic reactions in our model, e.g. $x\text{Li}^+ + x e^- + \text{C}_6 \rightarrow \text{Li}_x \text{C}_6$ and $\text{Li}^+ + e^- \rightarrow \text{Li}$, we adopt the coupled ion-electron transfer theory (CIET) for ion intercalation and Marcus-Hush-Chidney(MHC) kinetics for lithium plating/stripping.^{55,56} Coupled ion-electron transfer theory describes the concerted process of electron transfer and ion transfer across the solid-liquid interface for intercalation materials.⁵⁵ Using a simplified formula previously developed for the Marcus-Hush-Chidney kinetics,⁵⁶ the rate equation for CIET can be cast without the explicit integral of the electron's density of states as

$$i = k_0(1-x) \left(\frac{\tilde{c}_+}{1 + e^{\tilde{\eta}_t}} - \frac{x}{1 + e^{-\tilde{\eta}_t}} \right) \text{erfc}(f(\tilde{\lambda}, \tilde{\eta}_t)). \quad [7]$$

Here, k_0 is the rate constant in units of mA/cm^2 , $\tilde{c}_+ \equiv c_+/c_{\text{ref},+}$ is the electrolyte concentration normalized by reference electrolyte concentration $c_{\text{ref},+} = 1\text{M}$, and $\tilde{\lambda} \equiv \lambda/k_B T$ is the reorganization free energy λ from Marcus theory⁵⁷ normalized by the thermal energy $k_B T$. The overpotential η is the stoichiometry difference of electrochemical potentials between reactants and products,³⁸ while Eq. 7 adopts the usage of normalized formal overpotential $\tilde{\eta}_t \equiv \eta - k_B T \ln(x/\tilde{c}_+)$. An Ohmic potential drop iR_{film} shall also exist in η if resistance of solid electrolyte interphase is present. In short, the overpotential η with intercalation reaction as the forward direction is given as

$$e\eta = \mu_s + e(\phi_s - \phi_l^r) - iR_{\text{film}}. \quad [8]$$

Here, μ_s is the chemical potential of the reduced state in solid form, ϕ_s is the electrostatic potential in the solid, and ϕ_l^r represents the electrochemical potential of lithium ion using the voltage measured with respect to a lithium metal reference electrode locally.⁴⁸ The arise of the complementary error function $\text{erfc}(f)$ is to approximate the integral over electron's density of states involved in electron transfer theory, in which f is given as $f(\tilde{\lambda}, \tilde{\eta}_t) \equiv (\tilde{\lambda} - \sqrt{1 + \tilde{\lambda}^{1/2} + \tilde{\eta}_t^2}) / (2\tilde{\lambda}^{1/2})$. In Eq. 7, the $(1-x)$ prefactor originates from the assumption of the transition state of ion transfer that excludes one empty site near interface.⁵⁵ This simplified formula avoids the numerical integral of electron's state density needed in the original Marcus-type theory, leading to a non-Tafel behavior in high overpotential region (e.g. $\eta > 0.1\text{ V}$). For the purpose of comparison, we also adopt the widely used Butler-Volmer kinetics for ion intercalation in the following form

$$i = k_0 \tilde{c}_+^{1-\alpha} (1-x)^{1-\alpha} x^\alpha \left[\exp\left(\frac{\alpha}{k_B T} \eta\right) - \exp\left(-\frac{1-\alpha}{k_B T} \eta\right) \right]. \quad [9]$$

Here, $\alpha \in (0, 1)$ is the charge transfer coefficient and η is similarly defined as in Eq. 8. Although the two kinetic models can be similar when $\eta < 0.1\text{ V}$ by adjusting α ,⁵⁵ we note that CIET has a reaction rate asymmetry about $x = 0.5$ by derivation, while BV kinetic model relies on the fitted charge-transfer coefficient α to become asymmetric for intercalation materials.

A closed-form Marcus-Hush-Chidney(MHC) kinetics similar to Eq. 7 is adopted for lithium plating/stripping as following

$$i_{\text{pl}} = k_{0,\text{plating}} \left(\frac{\tilde{c}_+}{1 + e^{\tilde{\eta}_{\text{pl}}}} - \frac{1}{1 + e^{-\tilde{\eta}_{\text{pl}}}} \right) \text{erfc}(f(\tilde{\lambda}, \tilde{\eta}_{\text{pl}})) \quad [10]$$

Here, the dependence on concentration of reduced state, i.e. x in brackets and the prefactor $1-x$ of Eq. 7, is dropped because no transition state with excluded volume effect is needed for metal deposition. $k_{0,\text{plating}}$ is the exchange current density for lithium plating/stripping reactions. Following our previous work of lithium plating on single graphite particle,²⁶ a nucleation barrier $e\phi_{\text{nuc}}$ is introduced in the overpotential of plating reaction η_{pl} so that

$$\eta_{\text{pl}} \equiv \mu_{\text{Li}} + e\phi_{\text{nuc}} \exp(-V_{\text{Li}}/V_{\text{ref}}) + e(\phi_s - \phi_l^r) - iR_{\text{film}}. \quad [11]$$

The exponential decay of nucleation barrier depends on the ratio of the volume of plated lithium V_{Li} and a reference volume V_{ref} estimated from the nucleation theory to smoothly switch the plating process from a nucleation regime to a growth regime.^{26,58} In the following simulation, lithium plating is assumed to initiate only on outer surfaces of secondary graphite and treated as a reaction in parallel with the intercalation reaction. Equation 10 is also used for lithium stripping on the lithium foil counter electrode but without nucleation barrier.

Results of Li/Graphite Half-Cells

We parameterize our model to simulate Li/graphite half cells and compare them with experimental data under fast charging conditions to validate our model.⁸ C-rate notation is adopted to represent the lithiation condition. For instance, “4C” means applying a constant current to lithiate a graphite electrode from empty to full in 1/4 h. Our model resolves the hierarchical transport resistance and reaction resistance properly, and therefore, consistently captures the voltage profiles and the plating onset of all half cells. The spatial and temporal dynamics of lithiation of porous graphite electrodes are further revealed from simulations.

Experiments of Li/graphite half cells.—We validate our model against the dataset utilizing SLC1506T graphite from Superior Graphite for four reasons. First, it covers a wide range of charging conditions from 2C to 6C and two different areal capacities, i.e. 3.1 mAh cm^{-2} and 2.1 mAh cm^{-2} .^{8,59} We refer to cells of areal capacity 3.1 mAh cm^{-2} and 2.1 mAh cm^{-2} as thick cells and thin cells, respectively. Second, reliable estimations of onset of lithium plating under constant temperature conditions are available by a combination of OCV rest, coulombic efficiencies deviation, and gas evolution titration.⁸ Third, the morphology of secondary graphite particles for SLC1506T, including particle sphericity, particle size distribution, and BET surface area,^{32,44,60} are well characterized, greatly reducing the number of fitting parameters needed for simulations. Lastly, for data under each condition, at least three cells are repeated to minimize variations from individual cell. The electrolyte used in these cells is 1.2 M LiPF_6 in 3:7 EC(ethylene carbonate):EMC(ethyl methyl carbonate). We refer details of coin cell manufacture and electrochemical protocols to the original experimental work.⁸

Parameterization of model for Li/graphite half-cells.—Most parameters of our model are derived from either experimental characterizations or ab initio calculations. In addition to the chemical potential and diffusivity in graphite discussed in Simulation Model Section, material parameters associated with the morphology of SLC1506T graphite particles such as particle size distribution and BET surface area are obtained through independent characterizations and directly input into the model without fitting.^{32,60} Specifically, the particle size distribution of SLC1506T shown in Fig. 3 is discretized into 15 intervals evenly between $1\text{ }\mu\text{m}$ and $16\text{ }\mu\text{m}$. In other words, within each subvolume of the electrode, 15 particles are simulated.

Reaction rate related parameters for both ion intercalation using CIET model and lithium plating/stripping using MHC model are all estimated from experiments prior to fitting.^{26,61} For transport properties of electrolytes in both electrode scale and particle scale, we adopt experimentally measured bulk transport properties for LiPF_6 in EC/EMC in simulations. Expressions are available in MPET repository³⁷ and references.⁶² The porosities and tortuosities through porous structures at both electrode and particle scale have to be fitting parameters in practice because they are subject to the calendaring process and the cell's internal pressure. Empirical correction for effective transport properties through porous media based on Bruggeman's relation has been proposed by combining experiments and simulations and serves as initial input to our model.⁶³

We therefore have to use part of the experimental data to determine the remaining fitting parameters such as particle porosity and electrode tortuosity. Specifically, voltage profiles in thick cells (3.1 mAh cm^{-2}) under 3C and 4C conditions are used to determine all fitting parameters by matching both voltage profiles and onset of lithium plating. High current data are preferable in parameterization because they explore the nonlinear resistance from reactions and diffusion in the hierarchical structure and therefore are sensitive to model parameters. Furthermore, plating onset is sensitive to the small variation of resistance because it marks when the local electrode voltage drops below 0V with respect to lithium metal; A 10mV difference in voltage profiles can lead to a shift of plating onset by $\sim 5\%$. Parameters for simulations are summarized in Table I. Given the number of fitting parameters, this parameterization process is feasible and reliable in our model because all parameters have been individually constrained to a narrow window prior to parameterization. A comprehensive list of parameters with sources for initial estimation can be found in SI. To further demonstrate the sensitivity of model, a comprehensive set of simulations is presented in SI by varying each parameter individually.

Simulation results of Li/graphite half cells.—Our main results are summarized in Fig. 4, showing the comparison of voltages from simulation and experiments of both thick cells and thin cells. The electrode state of charge(SOC) from 0 to 1 corresponds to discharging of half cells and represents the empty and full states of graphite electrode, respectively. The voltage is the difference between two current collectors. Negative voltage means that the cell needs an extra voltage input to maintain the current. Experimentally, the onset points of lithium plating are estimated from multiple coulombic efficiency measurements (black rectangles). While in simulations, the local overpotential η_{pl} for lithium plating is used to determine the onset of lithium plating(colored rectangles), i.e. when $\eta_{\text{pl}} < 0$.

Table I. Parameters for porous graphite electrodes of SLC1506T.⁸

Parameter	Value
ϵ^s, τ^s	0.55, ⁸ 3.11(2.18) ^{a)}
ϵ^e, τ^e	0.382(0.374), ⁸ 5.30(4.36) ^{a)}
ϵ^p, τ^p	0.035, ⁶⁴ 0.035 ^{-1.35}
$D_{10}, D_{50}, D_{90}/\mu\text{m}$	5.1, 8.1, 12.6 ³²
$a/\mu\text{m}^2 \mu\text{m}^{-3}$	3.5 ^{32,65}
$k_0/\text{mA cm}^{-2}$	4.8 ^{CIET} (0.26 ^{BV})
α	0.3 ⁶⁶
$\lambda/k_B T$	5.0
$R_{\text{film}}/\Omega \text{ cm}^2$	15 ^{67,68}
$k_{0,\text{plating}}/\text{mA cm}^{-2}$	10 ⁶¹
$\lambda_{\text{plating}}/k_B T$	11.7 ⁶¹
$\phi_{\text{nuc}}/\text{mV}$	12 ⁵⁸

a) Values outside and inside parenthesis are for cell of capacity 3.1 mAh cm^{-2} and 2.1 mAh cm^{-2} , respectively.

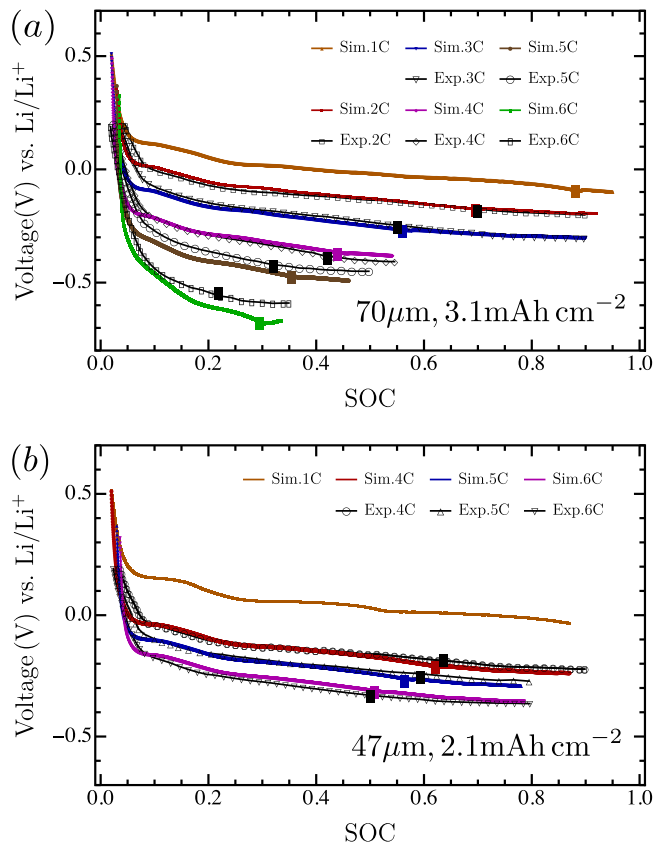


Figure 4. Simulated and measured voltage profiles and lithium plating onset points of Li/graphite half cells under 1C-6C constant current lithiation condition show strong agreement consistently. Graphite electrodes have areal capacity 3.1 mAh cm^{-2} in (a) and 2.1 mAh cm^{-2} in (b). The onset state of charge(SOC) of lithium plating for each lithiation condition is marked by colored solid rectangles for simulations and black solid rectangles for experiments.

Using parameters determined from fitting data of thick cells, our model can both track each of their corresponding experimental voltage profile closely and track the onset of lithium plating. As current increases from 2C to 6C, the voltage shifts downward mainly due to the electrolyte conduction limitation at the electrode scale. Deviations from experiments at low stage of charge (SOC < 0.1) is expected as our model approximates all low concentration phases as solid solution materials. Once the majority of graphite particles enter the Stage III-II coexistence region, i.e. $0.3 < x < 0.5$, voltages decrease more gradually as a result of phase separation. Unlike the single graphite particle under fast charging, where applied voltage changes rapidly due to phase-separation,²⁶ this gradual decrement is the average results of all particles in different phase morphologies. For low rates, such as 1C and 2C, the transition of slope, i.e. differential capacity dQ/dV , is observable when SOC ≈ 0.2 due to the phase-separation effect in graphite. While in high rates, such as 5C and 6C, the voltage profile has less noticeable transition at SOC ≈ 0.2 because three phases with different redox potentials, i.e. Stage III, II, and I, coexist in the porous graphite electrodes. Surprisingly, the difference of onset of lithium plating between simulations and experiments is only within few percentages of SOC; translating it to the difference in time is less than 30 s. This consistency holds up to 5C, resulting from properly resolved resistances from two-level hierarchical transport and dynamic faradaic reactions of multiple phases. A delayed plating onset and deviated voltage profile for 6C predicted by the model is primarily due to the limitation of volume averaging when concentration polarization in electrodes is strong.

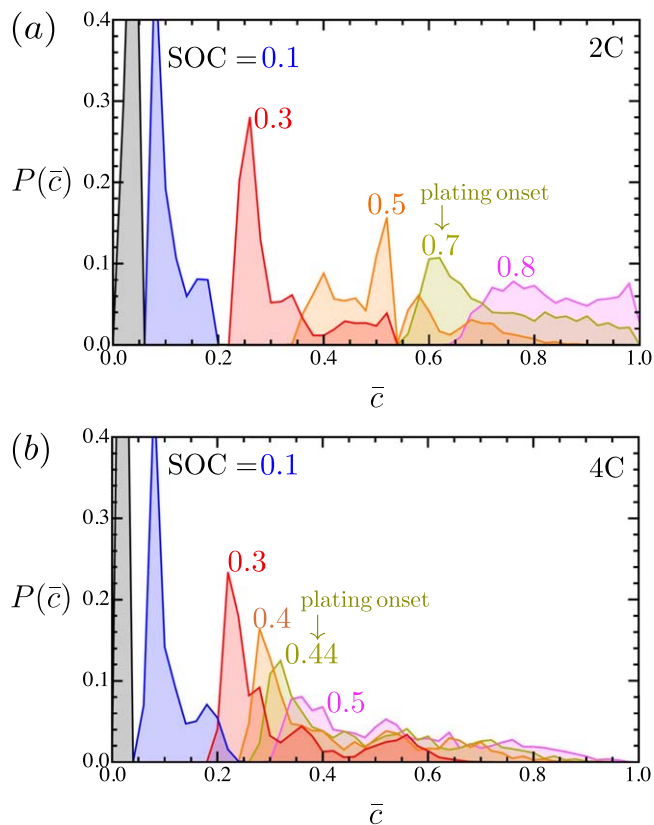


Figure 5. Distribution $P(\bar{c})$ of particle average concentration \bar{c} displays a narrow spread at low SOC prior to phase separation and a long tail at higher SOC due to phase-separation enhanced lithiation inhomogeneities. Results are shown for cells of 3.1 mAh cm^{-2} at various electrode state of charge (SOC) under (a) 2C and (b) 4C lithiation conditions.

The agreement of simulations and experiments in Fig. 4b for thin cells having areal capacity 2.1 mAh cm^{-2} is even more remarkable, given that parameters related to graphite materials were independently determined in cells of 3.1 mAh cm^{-2} . We note that the only different parameters in simulation between Figs. 4a and 4b are the tortuosities of separator and graphite electrodes. All other material related parameters remain the same in both Figs. 4a and 4b. Because the effective ionic transport resistance depends weakly on the state of charge, the tortuosities can be obtained by fitting voltage of the fastest profiles only without further fitting the plating onset in thin cells. As shown in Fig. S4, the effect of tortuosity on fitting is most apparent in the high current condition where ionic transport resistance limits the charging process. We hypothesize that this difference of tortuosities of the porous separators and porous electrodes are due to the variation of internal pressure within coin cells and calendaring process of electrodes. We note that the difference of fitted tortuosities is small compared to variation measured experimentally.^{69,70}

The simulated voltage profiles in Fig. 4b for thin cells exhibit more apparent transition of slope dQ/dV near $\text{SOC} \approx 0.2$ even under 6C condition, which is consistent with experiments. This is because three phases coexisting is less significant in thin cells due to their lower transport resistance in the electrode scale. The agreement of both voltage profiles and plating onset in Fig. 4b using material parameters determined from thick cells suggests the transferability of the model.

While multiphase-multiscale behavior of secondary graphite particle is the most significant characteristic of our model, the particle size distribution is also important to the model accuracy and transferability. Figure 5 shows the distribution of particle average concentration $\bar{c} \equiv 4\pi \int c(r)r^2 dr/V$ during 2C and 4C charging of

thick cells at various electrode SOC. Before significant phase-separation occurs, i.e. $\text{SOC} < 0.3$, the average concentration \bar{c} of particles has a relatively narrow distribution. A long tail distribution is observed when $\text{SOC} \geq 0.3$, demonstrating the inhomogeneous lithiation of graphite in the whole electrode enhanced by the phase-separation. Simulations using few particles may be still able to capture voltage profiles in a consistent way but lack the ability to resolve voltage difference at the order of 10mV and thereby to predict plating onset.

The nucleation barrier for lithium plating on graphite surfaces in simulations is consistently found to be at the order of $\sim 0.01 \text{ V}$ in all explored current conditions, in contrast to $\sim 0.1 \text{ V}$ found in previous experimental study using single crystal graphite²⁶ and copper current collector under high current conditions.⁵⁸ This is because the plating current in porous graphite electrodes is small initially as the graphite electrode still undertakes the most current near the plating onset due to its porous structure. This is therefore analogous to a low plating current on current collector, which has only a small nucleation barrier about 5 mV observed experimentally.⁵⁸ Without explicitly tracking the morphology change of plated lithium, our kinetic model of lithium plating takes the experimentally measured exchange current density, i.e. 10 mA cm^{-2} ,⁶¹ allowing simulations to consistently track all experimental voltage profiles closely even after plating occurs.

Simulations using Butler-Volmer(BV) kinetics are parameterized similarly with results presented in Fig. S1. The different parameters are the rate constant k_0 and charge transfer coefficient α , which are obtained by matching reaction rate of two kinetics at $1M$ electrolyte concentration and in the low overpotential limit, i.e. $\eta \rightarrow 0$. It is worth noting that the obtained exchanged current density and asymmetric charge-transfer coefficient $\alpha \approx 0.3$ are very close to the experimentally measured ones from single graphite particle.⁶⁶ Both BV and CIET kinetic models can therefore generate similar voltage profiles and prediction of plating onset as shown in Fig. S1 because the reaction overpotential under the explored experimental conditions is only about $3k_B T/e \approx 0.078 \text{ V}$, at which non-Tafel behavior is weak.

Spatial and temporal lithiation dynamics of porous graphite electrodes revealed by simulations.—To further demystify the dynamic faradaic resistances in the porous graphite electrodes, the lithiation dynamics of representative particles in thick electrodes (3.1 mAh cm^{-2}) under 1C, 3C and 4C conditions are presented in Fig. 6. We focus on the particles closest to the separator, where lithium plating is expected to initiate. The temporal variation of particles' currents due to phase-separation effect, size differences, and the particle porosity are presented and discussed.

The lithiation dynamics of particles next to the separator display distinct behaviors under low-current and high-current conditions. The volume fraction of different phases, e.g. stage III, II, and I, for all particles located in the distance $0\text{--}12 \mu\text{m}$ from the separator is presented in Fig. 6b. Under the 1C lithiation current, the volume fraction of stage III and II remains saturated after complete transformation for approximately 5% SOC (180 seconds) and 20% SOC (720 seconds), respectively. In these idle regimes, further lithiating graphite particles at a deeper depth that have not been fully transformed to stage II has a lower resistance comparing to the free energy barrier of forming stage I. While under 4C lithiation current, the whole electrode could not afford the current without immediately invoking further intercalation of the frontal particles to form stage I. These variations stem from the small difference between redox potentials of Li_xC_6 during the coexistence of stage I–II and that of stage II–III, e.g. $\sim 40 \text{ mV}$. Two different temporal lithiation dynamics have been reported in the *operando* XRD experiments previously²³ and captured theoretically here for the first time.

Solid concentration profiles and currents of representative particles with radii $R = 2.1, 4.1, \text{ and } 6.1 \mu\text{m}$ close to the separator are shown in Video S1, S2 and Fig. 6 for snapshots of the chosen

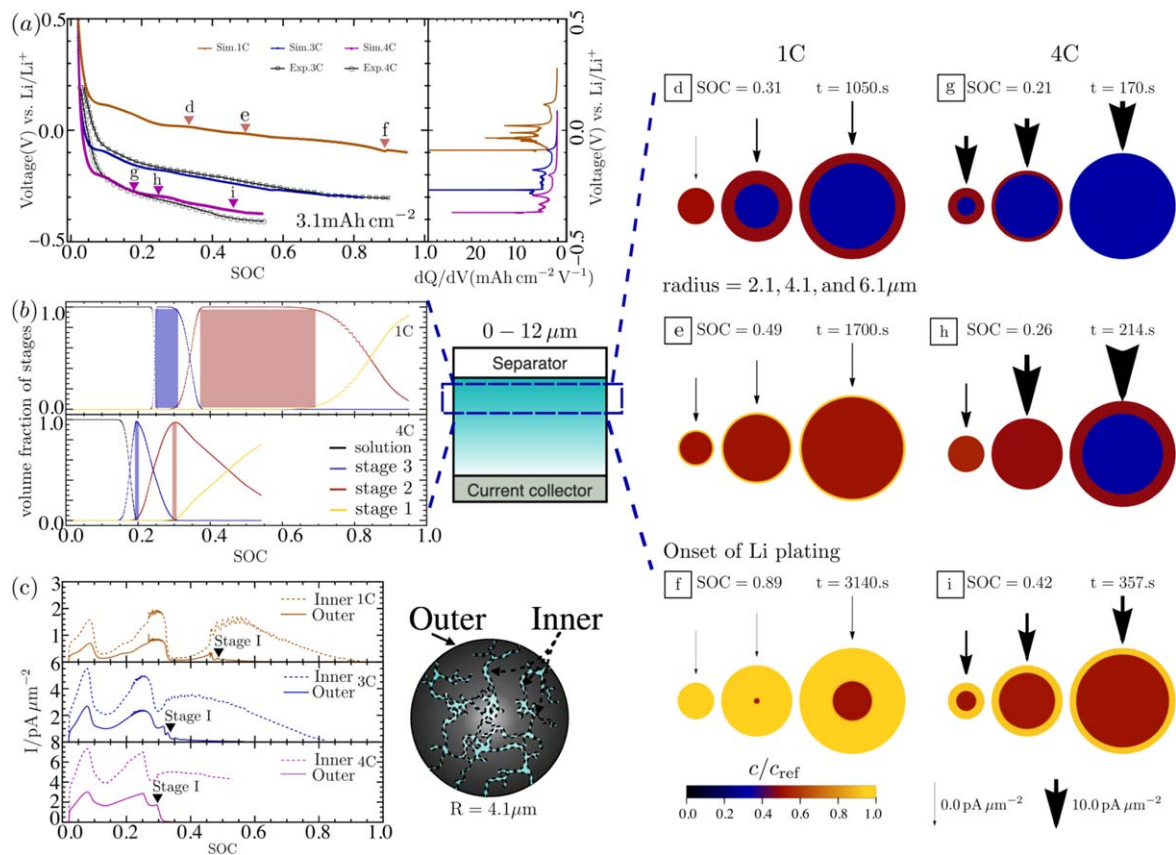


Figure 6. Dynamical phase morphologies in the electrode and particle scales of Li/graphite half-cell of areal density 3.1 mAh cm⁻². (a) Voltage profiles and the corresponding differential capacity dQ/dV under 1C, 3C and 4C conditions. (b) Evolution of the volume fraction of stage III, II and I in a distance 0–12 μm away from the separator shows two different current dependent temporal behavior. (c) Contributions of outer surface and inner surface to the current of a particle close to separator with radius $R = 4.1 \mu\text{m}$ under 1C, 3C and 4C lithiation conditions. Currents through outer surface diminishes upon the formation of stage I. (Right Column) representative concentration profiles of graphite particles with radii $R = 2.1, 4.1$, and $6.1 \mu\text{m}$ close to the separator under 1C(def) and 4C(ghi) lithiation condition. Arrow size indicates the transient current of the corresponding particle.

state of charge under 1C in Fig. 6(def) and 4C in Fig. 6(ghi). The size of arrow on top of each particle represents the particle's transient areal current density due to intercalation through both solid pathway and liquid pathway, which is the total current from this particle divided by its outer surface area. This is not to be confused with the current per unit area of the electrode sheet. The maximum magnitude of particle areal current density is about $15 \text{ pA } \mu\text{m}^{-2} = 1.5 \text{ mA cm}^{-2}$ under 4C, which is similar to the current quantified from *in-operando* XRD experiment using similar graphite materials.²³

When particles are experiencing phase-separation, the areal current density of particles are comparable regardless of particle size, which can be seen from Fig. 6e under 1C for Stage II–I coexistence and Fig. 6g under 4C for Stage III–II coexistence. Therefore, smaller particles are generally filled up earlier because of their lower particle's capacity. In Fig. 6d of 1C and Fig. 6h of 4C, while the larger particles is lagging behind in transition to become fully Stage II, the smaller particles have been fully transformed to the stage II. Meanwhile, the completely transformed Stage II particles provide smaller areal current density due to the free energy barrier for further lithiation to form the stage I and effectively remain idle for a period of time depending on currents. Figures 6f and 6i are extracted at the onset point of lithium plating under 1C and 4C conditions, respectively. As lithium plating occurs under 4C fast charging conditions, the graphite particles next to the separator are still far away from being completely transformed to Stage I, which qualitatively agrees with *in-operando* XRD experiment.²³

Figure 6c shows respective currents through inner surfaces and outer surfaces for a particle of radius $R = 4.1 \mu\text{m}$ as a function of the

electrode state of charge under 1C, 3C and 4C conditions. Although relatively small particle porosity considered in this work ($\epsilon^p = 3.4\%$),⁷¹ the liquid pathway contributes about 3 times more currents than the solid way for two reasons. First, the ionic transport resistance through liquid in micropores are lower than the solid transport even at such a low particle porosity. Second, substantial ion insertions take place at the exposed phase boundaries owing to the lower reaction resistance at the phase-boundary. This is the distinct difference between a single crystal graphite described by Eq. 2 and a secondary graphite particle described by Eq. 3.

Furthermore, the evolution of currents through outer surfaces and inner surfaces are always synchronized until the formation of Stage I. Slow diffusion in Stage I ($x > 0.9$) as a result of low solid diffusivity in Fig. 2 leads to the accumulation of a concentration gradient beneath the outer surface of graphite. This in turn further restricts the solid pathway as $x \rightarrow 1.0$ on the surface. We further notice that the voltage profiles and lithium plating onset shown in Fig. S6 are minimally affected by enhancing or reducing solid diffusivity globally by 5 times, indicating no solid diffusion limitation before the formation of stage I. Therefore, we speculate that solid diffusion limitation during fast charging in secondary graphite particles becomes substantially only upon the formation of stage I, a challenge that can be alleviated by increasing the particle porosity.

Electrochemical features of lithium plating.—Various electrochemical features have been suggested to monitor the lithium plating on graphite, such as the extreme of voltage,⁷² differential capacity analysis(dQ/dV),⁶ resistance change by current pulse⁴ and

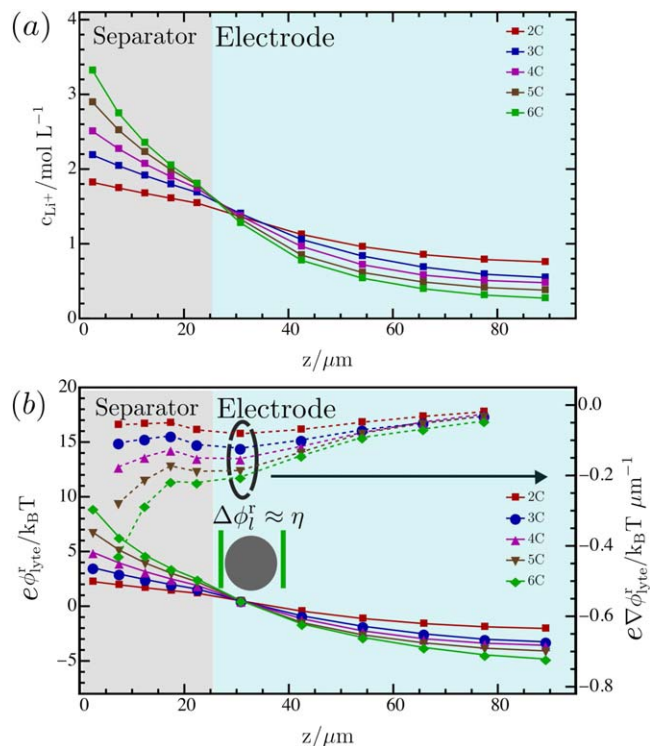


Figure 7. (a) Electrolyte concentration and (b) the electrochemical potential of Li^+ in electrolyte, i.e. ϕ_i^r in Eq. 8 across the electrode taken at the respective lithium plating onset in a 3.1 mAh cm^{-2} electrode under 2C to 6C charging condition. Across the surface of a secondary graphite particle with diameter about $10 \mu\text{m}$, the variation of c_+ electrolyte concentration, e.g. $\sim 1\text{M}$, and ϕ_i^r the electrochemical potential of Li^+ , e.g. $\sim 2k_B T$, are not negligible under 6C.

electrochemical impedance spectroscopy.² These features are usually easy to measure, however, difficult to interpret in practice without a proper model. At the core of these features is that the overall anode resistance starts to decrease once the lithium plating begins as it allows extra faradaic reactions that are easier than further intercalation of graphite.

Our simulation results reproduce some of these features and provide insight into them. In the 1C lithiation current, a hump due to the nucleation barrier of lithium plating can be observed at the state point f indicated in Fig. 6a, which has also been observed experimentally.⁶ Given the magnitude of nucleation barrier under typical charging currents, e.g. 10 mV, the hump can be easily overridden by the rapid resistance change of intercalation into graphite. It becomes less noticeable in the 3C case and completely hidden in 4C case. The minimum potential of graphite electrode was also previously argued to be an indicator of lithium plating.^{4,72} Depending on how much current lithium plating reaction contributes to the total current, this voltage minimum due to the resistance reduction from lithium plating may not be able to promptly detect lithium plating. For the 4C current in Fig. 6a, voltage keeps decreasing after plating onset at state i and no voltage minimum is observed within following 10% SOC either in experiments or simulation. The peaks of dQ/dV ⁶ and IR drop⁴ can be more sensitive indicators because they all reflect the resistance change promptly. Figure 6a presents dQ/dV calculated from the voltage profiles, showing several peaks arising from phase-separation in graphite and lithium plating. We note that these electrochemical features are less observable in the full cell setting owing to the resistance change from cathode. Our work therefore provides an alternative to estimate plating onset in full cells with additional modeling effort on cathode materials.

Limitation and perspective of porous electrode theory.—Lastly, the limitation and needed correction of porous electrode theory based model for extremely fast charging are discussed. In Fig. 4a, the apparent deviation of the simulation and the experiment of the thick electrode (3.1 mAh cm^{-2}) under 6C lithiation current arises from the approximation of uniform electrolytes outside each particle. Figure 7 quantitatively demonstrates the build up of gradient of concentration and electrochemical potential of Li^+ across the electrode under varying currents from 2C to 6C for the thick electrode (3.1 mAh cm^{-2}). Profiles of electrolyte concentration c_+ and electrochemical potential ϕ_i^r for Li^+ for each condition are taken at their respective plating onset points. Within the first $10 \mu\text{m}$ of the electrode, under 6C lithiation condition, the variation of electrolyte concentration is about 1M and that of electrochemical potential ϕ_i^r for Li^+ is about $2k_B T$, which is similar to the overpotential η for intercalation reactions. Therefore, to model further faster charging involving steeper concentration polarization, the model needs to be modified to capture the variation of the electrochemical potential ϕ_i^r of Li^+ on the surface of particle rather than taking the approximation of uniform electrolyte as in Eq. 6.

Conclusions

A hierarchical multiphase porous electrode theory has been formulated and is applied to porous graphite electrodes. It resolves the effects of electrochemically driven phase separation and transport in hierarchical pore structures characterized by multiscale porosity and secondary particle size distributions. We validate our model extensively against a rich set of experiments using Li/graphite half cells. The parameters of the model, especially those related to material morphology and reaction kinetics, have been rigorously constrained by independent experimental sources before fitting and have been found to be transferable to cells with different thickness. Simulated voltage profiles exhibit unprecedented consistency and accuracy when compared to experiments under various fast charging, varying from 2C to 6C. A major contribution of the model is that simulations consistently predict the onset of lithium plating with strong agreement to experiments. Lithium plating predictions and measurements differ at most by a few percentages of electrode state of charge, which translates to a difference in time of less than 30 s. Therefore, our model has the potential to be used for model-based design of cycling protocols and electrode microstructures.

Our simulations reveal the lithiation dynamics, showing how populations of particles in different phase morphology contribute to the total current. Two key features of lithiation dynamics are observed: (1) during lithiation, the time for graphite remaining in stage II depends on the current, qualitatively matching the lithiation dynamics measured using in-operando XRD experiments;²³ (2) the formation of stage I stops further ion insertion through solid pathway and reduces the current from that particle by about 1/3 in the electrodes we investigated. The dominant contribution of currents from inner surfaces of particles suggests the possibility of achieving fast charging by optimizing particle porosity and improving reaction kinetics. Simulation results provide insights for promptly detecting lithium plating using peak of differential capacity dQ/dV . We identify the limitation of porous electrode theory based model in modeling strong concentration polarization and propose the needed improvement. Finally, our model featuring a phase-field model of porous graphite particle is broadly applicable to other graphite morphologies and both phase-separable and non phase-separable materials possessing hierarchical porous structure, including but not limited to $\text{Li}_4\text{Ti}_5\text{O}_{12}$, LiCoO_2 , and $\text{LiNi}_x\text{Mn}_y\text{Co}_{1-x-y}\text{O}_2$.

Acknowledgments

This work was supported by the Toyota Research Institute through D3BATT: Center for Data-Driven Design of Li-Ion

Batteries. H.L. would like to express gratitude to Dr. Huanhuan Tian for valuable discussions and to Alexander E. Cohen for proof-reading.

ORCID

Huada Lian  <https://orcid.org/0000-0003-3564-3535>

References

- P. P. Paul et al., "A review of existing and emerging methods for lithium detection and characterization in li-ion and li-metal batteries." *Adv. Energy Mater.*, **11**, 2100372 (2021).
- D. E. Brown, E. J. McShane, Z. M. Konz, K. B. Knudsen, and B. D. McCloskey, "Detecting onset of lithium plating during fast charging of li-ion batteries using operando electrochemical impedance spectroscopy." *Cell Reports Physical Science*, **2**, 100589 (2021).
- L. Xu et al., "Operando quantified lithium plating determination enabled by dynamic capacitance measurement in working li-ion batteries." *Angew. Chem. Int. Ed.*, **61**, e202210365 (2022).
- L. Xu, Y. Yang, Y. Xiao, W. L. Cai, Y. X. Yao, X. R. Chen, C. Yan, H. Yuan, and J. Q. Huang, "In-situ determination of onset lithium plating for safe li-ion batteries." *Journal of Energy Chemistry*, **67**, 255 (2022).
- S. S. Zhang, "The effect of the charging protocol on the cycle life of a li-ion battery." *Journal of power sources*, **161**, 1385 (2006).
- B. Ma, S. Agrawal, R. Gopal, and P. Bai, "Operando microscopy diagnosis of the onset of lithium plating in transparent lithium-ion full cells." *ACS Applied Materials & Interfaces*, **14**, 54708 (2022).
- A. Adam, E. Knobbe, J. Wandt, and A. Kwade, "Application of the differential charging voltage analysis to determine the onset of lithium-plating during fast charging of lithium-ion cells." *Journal of Power Sources*, **495**, 229794 (2021).
- Z. M. Konz, B. M. Wirtz, A. Verma, T. Y. Huang, H. K. Bergstrom, M. J. Crafton, D. E. Brown, E. J. McShane, A. M. Colclasure, and B. D. McCloskey, "High-throughput li plating quantification for fast-charging battery design." *Nat. Energy*, **8**, 450 (2023).
- J. Burns, D. Stevens, and J. Dahn, "In-situ detection of lithium plating using high precision coulometry." *J. Electrochem. Soc.*, **162**, A959 (2015).
- W. Huang et al., "Onboard early detection and mitigation of lithium plating in fast-charging batteries." *Nat. Commun.*, **13**, 7091 (2022).
- F. B. Spingler, W. Wittmann, J. Sturm, B. Rieger, and A. Jossen, "Optimum fast charging of lithium-ion pouch cells based on local volume expansion criteria." *Journal of Power Sources*, **393**, 152 (2018).
- K. M. Diederichsen, E. J. McShane, and B. D. McCloskey, "Promising routes to a high li+ transference number electrolyte for lithium ion batteries." *ACS Energy Lett.*, **2**, 2563 (2017).
- S. Malifarge, B. Delobel, and C. Delacourt, "Experimental and modeling analysis of graphite electrodes with various thicknesses and porosities for high-energy-density li-ion batteries." *J. Electrochem. Soc.*, **165**, A1275 (2018).
- P. Arora, M. Doyle, and R. E. White, "Mathematical modeling of the lithium deposition overcharge reaction in lithium-ion batteries using carbon-based negative electrodes." *J. Electrochem. Soc.*, **146**, 3543 (1999).
- S. Hein, T. Danner, and A. Latz, "An electrochemical model of lithium plating and stripping in lithium ion batteries." *ACS Appl. Energy Mater.*, **3**, 8519 (2020).
- K. Vikrant and S. Allu, "Modeling of lithium nucleation and plating kinetics under fast charge conditions." *J. Electrochem. Soc.*, **168**, 020536 (2021).
- A. M. Colclasure, A. R. Dunlop, S. E. Trask, B. J. Polzin, A. N. Jansen, and K. Smith, "Requirements for enabling extreme fast charging of high energy density li-ion cells while avoiding lithium plating." *J. Electrochem. Soc.*, **166**, A1412 (2019).
- J. Dahn, "Phase diagram of lixc6." *Physical Review B*, **44**, 9170 (1991).
- Y. Guo, R. B. Smith, Z. Yu, D. K. Efetov, J. Wang, P. Kim, M. Z. Bazant, and L. E. Brus, "Li intercalation into graphite: direct optical imaging and cahn-hilliard reaction dynamics." *The Journal of Physical Chemistry Letters*, **7**, 2151 (2016).
- R. B. Smith, E. Khoo, and M. Z. Bazant, "Intercalation kinetics in multiphase-layered materials." *J. Phys. Chem. C*, **121**, 12505 (2017).
- S. Weng et al., "Localized-domains staging structure and evolution in lithiated graphite." *Carbon Energy*, **5**, 1 (2022).
- X. Lu et al., "Multiscale dynamics of charging and plating in graphite electrodes coupling operando microscopy and phase-field modelling." *Nat. Commun.*, **14**, 5127 (2023).
- D. P. Finegan et al., "Spatial dynamics of lithiation and lithium plating during high-rate operation of graphite electrodes." *Energy & Environmental Science*, **13**, 2570 (2020).
- R. B. Smith and M. Z. Bazant, "Multiphase porous electrode theory." *J. Electrochem. Soc.*, **164**, E3291 (2017).
- J. Newman and W. Tiedemann, "Porous-electrode theory with battery applications." *AIChE J.*, **21**, 25 (1975).
- T. Gao, Y. Han, D. Fraggadakis, S. Das, T. Zhou, C. N. Yeh, S. Xu, W. C. Chueh, J. Li, and M. Z. Bazant, "Interplay of lithium intercalation and plating on a single graphite particle." *Joule*, **5**, 393 (2021).
- J. Lim et al., "Origin and hysteresis of lithium compositional spatiodynamics within battery primary particles." *Science*, **353**, 566 (2016).
- T. R. Fergusson and M. Z. Bazant, "Phase transformation dynamics in porous battery electrodes." *Electrochimica Acta*, **146**, 89 (2014).
- K. E. Thomas-Alyea, C. Jung, R. B. Smith, and M. Z. Bazant, "In situ observation and mathematical modeling of lithium distribution within graphite." *J. Electrochem. Soc.*, **164**, E3063 (2017).
- S. Ahn et al., "Chemical origins of a fast-charge performance in disordered carbon anodes." *ACS Appl. Energy Mater.*, **6**, 8455 (2023).
- D. Qu and H. C. Yu, "Multiphysics electrochemical impedance simulations of complex multiphase graphite electrodes." *ACS Appl. Energy Mater.*, **6**, 3468 (2023).
- V. Srinivasan and J. Andrew, "X-cel: extreme fast charge cell evaluation of lithium-ion batteries." *Project Report*, **1**, 1 (2018), <https://energy.gov/eere/vehicles/articles/extreme-fast-charge-cell-evaluation-lithium-ion-batteries-xcel-heat>.
- A. Eldesoky, M. Bauer, S. Azam, E. Zsoldos, W. Song, R. Weber, S. Hy, M. Johnson, M. Metzger, and J. Dahn, "Impact of graphite materials on the lifetime of nmc811/graphite pouch cells: Part i. material properties, are safety tests, gas generation, and room temperature cycling." *J. Electrochem. Soc.*, **168**, 110543 (2021).
- J. Kim, K. Park, H. Woo, B. Gil, Y. S. Park, I. S. Kim, and B. Park, "Selective removal of nanopores by triphenylphosphine treatment on the natural graphite anode." *Electrochimica Acta*, **326**, 134993 (2019).
- S. Dargaville and T. W. Farrell, "Predicting active material utilization in lifepo4 electrodes using a multiscale mathematical model." *J. Electrochem. Soc.*, **157**, A830 (2010).
- O. Birkholz and M. Kamlah, "Electrochemical modeling of hierarchically structured lithium-ion battery electrodes." *Energy Technology*, **9**, 2000910 (2021).
- MPET–Multiphase Porous Electrode Theory, open-source battery simulation software available at <https://github.com/TRI-AMDD/mpet>.
- M. Z. Bazant, "Theory of chemical kinetics and charge transfer based on nonequilibrium thermodynamics." *Acc. Chem. Res.*, **46**, 1144 (2013).
- M. Chandresis, D. Caliste, D. Jamet, and P. Pochet, "Thermodynamics and related kinetics of staging in intercalation compounds." *J. Phys. Chem. C*, **123**, 23711 (2019).
- D. Fraggadakis, N. Nadkarni, T. Gao, T. Zhou, Y. Zhang, Y. Han, R. M. Stephens, Y. Shao-Horn, and M. Z. Bazant, "A scaling law to determine phase morphologies during ion intercalation." *Energy & Environmental Science*, **13**, 2142 (2020).
- N. Nadkarni, T. Zhou, D. Fraggadakis, T. Gao, and M. Z. Bazant, "Modeling the metal-insulator phase transition in lixc02 for energy and information storage." *Adv. Funct. Mater.*, **29**, 1902821 (2019).
- S. Agrawal and P. Bai, "Operando electrochemical kinetics in particulate porous electrodes by quantifying the mesoscale spatiotemporal heterogeneities." *Adv. Energy Mater.*, **11**, 2003344 (2021).
- M. Heß and P. Novák, "Shrinking annuli mechanism and stage-dependent rate capability of thin-layer graphite electrodes for lithium-ion batteries." *Electrochimica Acta*, **106**, 149 (2013).
- S. Pidaparthi, M. T. F. Rodrigues, J. M. Zuo, and D. P. Abraham, "Increased disorder at graphite particle edges revealed by multi-length scale characterization of anodes from fast-charged lithium-ion cells." *J. Electrochem. Soc.*, **168**, 100509 (2021).
- K. Persson, Y. Hinuma, Y. S. Meng, A. Van der Ven, and G. Ceder, "Thermodynamic and kinetic properties of the li-graphite system from first-principles calculations." *Physical Review B*, **82**, 125416 (2010).
- D. Billaud and F. Henry, "Structural studies of the stage iii lithium-graphite intercalation compound." *Solid State Commun.*, **124**, 299 (2002).
- T. R. Fergusson and M. Z. Bazant, "Nonequilibrium thermodynamics of porous electrodes." *J. Electrochem. Soc.*, **159**, A1967 (2012).
- J. Newman and N. P. Balsara, *Electrochemical Systems* (Wiley, United States) (2021).
- Y. Zeng, P. Albertus, R. Klein, N. Chaturvedi, A. Kojic, M. Z. Bazant, and J. Christensen, "Efficient conservative numerical schemes for 1d nonlinear spherical diffusion equations with applications in battery modeling." *J. Electrochem. Soc.*, **160**, A1565 (2013).
- S. Lueth, U. S. Sauter, and W. G. Bessler, "An agglomerate model of lithium-ion battery cathodes." *J. Electrochem. Soc.*, **163**, A210 (2015).
- I. Mele, I. Pačnik, K. Zelič, J. Moškon, and T. Katrašnik, "Advanced porous electrode modelling framework based on more consistent virtual representation of the electrode topology." *J. Electrochem. Soc.*, **167**, 060531 (2020).
- Q. Liang and M. Z. Bazant, "Hybrid-mpet: an open-source simulation software for hybrid electrode batteries." (2023), [arXiv:2305.15599](https://arxiv.org/abs/2305.15599).
- V. Srinivasan and J. Newman, "Discharge model for the lithium iron-phosphate electrode." *J. Electrochem. Soc.*, **151**, A1517 (2004).
- S. Whitaker, *The method of volume averaging* (Springer Science & Business Media, United States) Vol. 13 (2013).
- D. Fraggadakis, M. McEldrew, R. B. Smith, Y. Krishnan, Y. Zhang, P. Bai, W. C. Chueh, Y. Shao-Horn, and M. Z. Bazant, "Theory of coupled ion-electron transfer kinetics." *Electrochimica Acta*, **367**, 137432 (2021).
- Y. Zeng, R. B. Smith, P. Bai, and M. Z. Bazant, "Simple formula for marcus-hush-chidsey kinetics." *Journal of Electroanalytical Chemistry*, **735**, 77 (2014).
- R. A. Marcus, "Chemical and electrochemical electron-transfer theory." *Annual Review of Physical Chemistry*, **15**, 155 (1964).
- A. Pei, G. Zheng, F. Shi, Y. Li, and Y. Cui, "Nanoscale nucleation and growth of electrodeposited lithium metal." *Nano Lett.*, **17**, 1132 (2017).
- E. J. McShane, A. M. Colclasure, D. E. Brown, Z. M. Konz, K. Smith, and B. D. McCloskey, "Quantification of inactive lithium and solid-electrolyte interphase species on graphite electrodes after fast charging." *ACS Energy Lett.*, **5**, 2045 (2020).
- F. L. Usseglio-Viretta, D. P. Finegan, A. Colclasure, T. M. Heenan, D. Abraham, P. Shearing, and K. Smith, "Quantitative relationships between pore tortuosity, pore topology, and solid particle morphology using a novel discrete particle size algorithm." *J. Electrochem. Soc.*, **167**, 100513 (2020).

61. D. T. Boyle, X. Kong, A. Pei, P. E. Rudnicki, F. Shi, W. Huang, Z. Bao, J. Qin, and Y. Cui, "Transient voltammetry with ultramicroelectrodes reveals the electron transfer kinetics of lithium metal anodes." *ACS Energy Lett.*, **5**, 701 (2020).
62. J. Landesfeind and H. A. Gasteiger, "Temperature and concentration dependence of the ionic transport properties of lithium-ion battery electrolytes." *J. Electrochem. Soc.*, **166**, A3079 (2019).
63. F. L. Usseglio-Viretta et al., "Resolving the discrepancy in tortuosity factor estimation for li-ion battery electrodes through micro-macro modeling and experiment." *J. Electrochem. Soc.*, **165**, A3403 (2018).
64. S. Sailer, M. Mundsinger, J. Martin, M. Mancini, M. Wohlfahrt-Mehrens, and U. Kaiser, "Quantitative fib/sem tomogram analysis of closed and open porosity of spheroidized graphite anode materials for libs applications." *Micron*, **166**, 103398 (2023).
65. M. Kim, D. C. Robertson, D. W. Dees, K. P. Yao, W. Lu, S. E. Trask, J. T. Kirner, and I. Bloom, "Estimating the diffusion coefficient of lithium in graphite: Extremely fast charging and a comparison of data analysis techniques." *J. Electrochem. Soc.*, **168**, 070506 (2021).
66. K. Dokko, N. Nakata, Y. Suzuki, and K. Kanamura, "High-rate lithium deintercalation from lithiated graphite single-particle electrode." *J. Phys. Chem. C*, **114**, 8646 (2010).
67. R. Guo and B. M. Gallant, "Li₂O solid electrolyte interphase: probing transport properties at the chemical potential of lithium." *Chemistry of Materials*, **32**, 5525 (2020).
68. I. Nicotera, G. A. Ranieri, M. Terenzi, A. V. Chadwick, and M. I. Webster, "A study of stability of plasticized peo electrolytes." *Solid State Ionics*, **146**, 143 (2002).
69. J. Landesfeind, J. Hattendorff, A. Ehrl, W. A. Wall, and H. A. Gasteiger, "Tortuosity determination of battery electrodes and separators by impedance spectroscopy." *J. Electrochem. Soc.*, **163**, A1373 (2016).
70. T. DuBeshter, P. K. Sinha, A. Sakars, G. W. Fly, and J. Jorne, "Measurement of tortuosity and porosity of porous battery electrodes." *J. Electrochem. Soc.*, **161**, A599 (2014).
71. J. Martin, P. Axmann, M. Wohlfahrt-Mehrens, and M. Mancini, "Lithium intercalation kinetics and fast-charging lithium-ion batteries: rational design of graphite particles via spheroidization." *Energy Technology*, **11**, 2201469 (2023).
72. C. Fear, T. Adhikary, R. Carter, A. N. Mistry, C. T. Love, and P. P. Mukherjee, "In operando detection of the onset and mapping of lithium plating regimes during fast charging of lithium-ion batteries." *ACS Applied Materials & Interfaces*, **12**, 30438 (2020).